Contactless Optical Packaging Concept for Laser to Fiber Coupling

Saood Ibni Nazir and Yves Bellouard

***Abstract*— A novel method for the laser to fiber coupling is presented in which coarse alignment is achieved through micromachined v-grooves and mirrors in a fused silica substrate. Furthermore, fine repositioning is done in a noncontact manner by using a femtosecond laser to induce localized nanoscopic volume changes in specific locations within the bulk of the substrate, which, once combined with monolithic flexures within the substrate, produces a highly controlled motion. Using this principle, we overcome inherent manufacturing/assembly tolerances to achieve near theoretical coupling efficiency in a permanent manner. This proof of concept demonstrates a novel packaging principle where a sub-nm positioning resolution is achieved over tens of micrometers range of motion, efficiently overcoming intrinsic manufacturing tolerances.**

***Index Terms*— Femtosecond laser machining, flexures, fused silica, integrated optics, laser beam steering, laser diode packaging, micro-optics, noncontact, repositioning, tunable optics.**

I. Introduction

In THE past decades, there has been a considerable research effort in the area of integrated photonic circuits. In particular, silicon photonics has ushered tremendous developments in telecommunication [1], quantum optics [2], sensing [3], and nonlinear optics [4], [5]. Yet, robust and cost-effective packaging solutions are still a major bottleneck in the commercialization of photonic integrated circuits (PICs) [6]. Integrating multiple functionalities on a single chip requires electrical, optical, mechanical, and thermal connections between a PIC and the outside world. Another key aspect of Si-photonics is the on-chip integration of the light source. One of the main challenges toward industrialization is the efficient coupling between single-mode fibers (SMFs) and nanometer-scale photonic waveguides on a PIC primarily due to their large mode mismatch. To solve this problem, a variety of strategies-edge coupling [7], vertical coupling [8], and evanescent coupling [9] have been developed although it remains a formidable challenge [6], [10], [11]. Depending on the approach, alignment tolerances are typically in the range of sub-μm–2.5 μm for a 1-dB loss [12]–[14]. Direct-write two-photon laser lithography [15], [16] overcomes many of these limitations. Using this technique, beam shaping elements such as lenses, prisms, and gratings can be 3-D printed onto facets of optical devices with unprecedented resolution [17], [18]. Tolerances are, however, still present due to a possible nonuniform shrinkage of the resist during development. Furthermore, the use of polymers poses long-term and environmental stability challenges. As such, for an overall integration, postassembly adjustments are, sometimes, indispensable to improve performance.

The integration of multiple optical elements, often with different material properties, on a single substrate is a challenging task requiring multiple steps of alignment and fixation with very tight tolerances. To fulfill these demands, device-specific packaging methods and tools are needed, further adding to the production cost of the overall device. In addition to tolerances inherently associated with the fabrication of the individual components, additional uncertainties add in during the assembly steps. This is particularly critical for devices with tight alignment tolerances, such as fiber-pigtailed laser diodes, fiber-coupled integrated photonic devices, alignment between whispering gallery modes (WGMs) of silica microspheres and waveguides, and fiber-to-chip and chip-to-chip interfaces. While these systems can be routinely aligned in a laboratory environment, for a fully packaged device, adjustments may be particularly difficult to realize and often create a bottleneck in the successful commercialization of such devices.

So far, we have briefly outlined the technical challenges associated with photonic integration on a single chip. In the following, we elaborate on this discussion further in the context of fiber pigtailed laser diodes for which we demonstrate a contactless method to achieve fiber injection. The methods presented are generic and of interest for a broader set of problems with similar alignment constraints.

Low-loss coupling between laser diodes and SMF is a common problem in both industry and academia. The challenge in doing so is embedded in the small size of a laser diode package and misalignments that can accumulate during the attachment of different components of the package. This could be due to a lack of accuracy in the tools used for positioning, fabrication tolerances of the individual components, or the fixation method itself. For example, fiber pigtailing usually involves laser welding, where postweld shifts (PWSs) can cause relative movements between prealigned components, resulting in a significant increase in the coupling loss. Although various strategies have been proposed to minimize PWS [19]–[21], suppressing PWS completely remains challenging nonetheless. In comparison to other assembly methods, such as adhesive

Manuscript received February 5, 2021; revised April 28, 2021; accepted May 11, 2021. Date of publication May 18, 2021; date of current version June 16, 2021. The Galatea Lab acknowledges the sponsoring of Richemont International. Recommended for publication by Associate Editor F. Shi upon evaluation of reviewers' comments. *(Corresponding author: Saood Ibni Nazir.)*

The authors are with School of Engineering, École polytechnique fédérale de Lausanne (EPFL), CH-2000 Neuchatel, Switzerland (e-mail: saood.nazir@epfl.ch).

Color versions of one or more figures in this article are available at https://doi.org/10.1109/TCPMT.2021.3080513.

Digital Object Identifier 10.1109/TCPMT.2021.3080513

bonding and gluing, laser welding offers better advantages in terms of precision, strength, and long-term stability. However, as an alternative, in [22], a multifiber array fixation using UV-curing with reproducibility of ±40 nm has been demonstrated. By varying the fiber–substrate distance, the authors have achieved a repeatable vertical shrinkage in the range of 100–220 nm.

Passive alignment using silicon etched v-grooves, solder bumps, and stops can offer up to ±1-μm transverse alignment precision [23], [24]; however, due to tolerances in micromachined components, fiber cladding-core concentricity tolerance, and so on, an additional active alignment step is required, significantly increasing the production cost. The integration of a movable micromirror inside the package has also received some attention [25]–[27]. Similarly, microelectromechanical system (MEMS)-based fiber positioning devices have also been demonstrated [28], [29]. While this certainly relaxes alignment tolerances required during assembly, it requires additional onboard electronics to dynamically control the actuation. In terms of postassembly correction, laser-forming offers a noncontact, sub-μm alignment approach [30], [31]. However, the process relies on linear absorption and, thus, can only be applied to the surface of materials, which limits the type of movements that can be produced.

In this work, we explore the concept of a monolithic fiber injection mechanism, fabricated by a femtosecond laser, and for which fine alignment is performed using the same laser. This is done by utilizing in-volume modifications resulting from femtosecond laser exposure [32] combined with monolithic flexures in a single fused silica substrate [33]. To this end, a 2-D beam steering mechanism is demonstrated in the context of high-precision laser-to-fiber injection to achieve high coupling efficiency in a reliable and permanent manner. A schematic of the workstation along with a brief description of the process is given in Fig. 1.

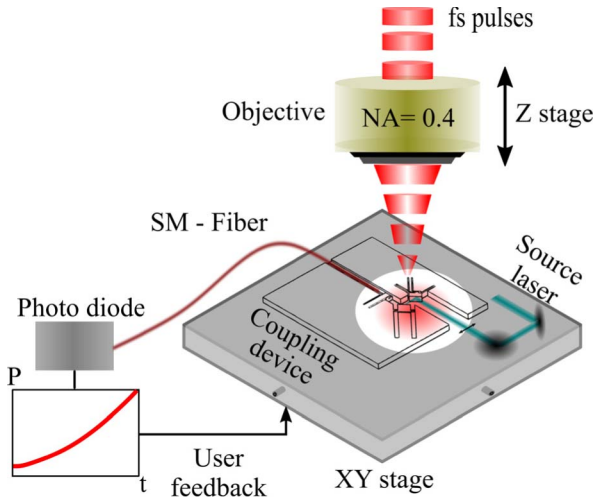

Fig. 1. Schematic of the experimental setup used to perform the noncontact alignment. The coupling device is positioned on an $x - y$ positioning stage and translated under the adjustable focus of a femtosecond laser beam under normal incidence. The laser-induced modifications are written in certain locations to create localized movements within the device, thus changing the coupling efficiency between the source laser beam and the fiber. While writing, the coupled power is monitored continuously at the other end of the fiber and used as a performance metric to guide the alignment process. An LED (shown in red) is mounted below to image different parts of the device during laser exposure.

II. Laser-to-Fiber Coupling Mechanism

A. Coupling Device Working Principle

The device, as shown in Fig. 2, consists of two adjustable mirrors that are positioned to guide the light from the laser source inside the glass chip. The mirrors are fabricated parallel to each other such that the incoming beam is shifted laterally. Further downstream from the second mirror, a v-groove is used to hold the fiber and passively align it with the center of the mirror. To fix the fiber, one end of it is clamped using a mechanical finger, which is monolithically integrated into the mechanism. The finger is a flexible cantilever that firmly clamps the fiber from the top, thus forcing it into the v-groove. For the sake of this demonstration, two homemade gold-coated optical flats are glued to the mirror surfaces. However, commercially available mirrors can be integrated too or by using a laser postprocessing step (CO_2 reflow for instance [34]); the surfaces could be smoothened down to sub-nm level without changing the repositioning principle. Presently, the surfaces have a roughness of the order of 100 nm (Ra) at best.

To couple the laser diode into the fiber, the output is first collimated and then refocused using a long-range objective.

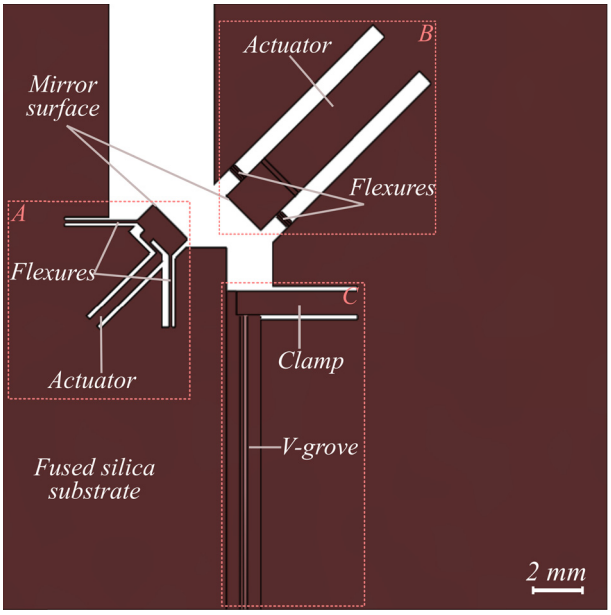

Fig. 2. Computer-assisted drawing (CAD) of the mechanism. The mechanism consists of three main parts. Parts A and B guide the laser diode on the fiber in addition to providing two degrees of freedom. Part C consists of a v-groove to hold the fiber and a flexible clamp to firmly hold it in place.

As shown in Fig. 3, aligning the incident beam at 45° on the first mirror (M_1), and adjusting the position of the objective along the z-direction, the beam is focused on the fiber. To scan the face of the fiber, the mirrors are tilted about their respective axes using femtosecond laser-assisted actuation, as will be described later on. The mirror M_1 is supported by a remote center of rotation (RCR) mechanism

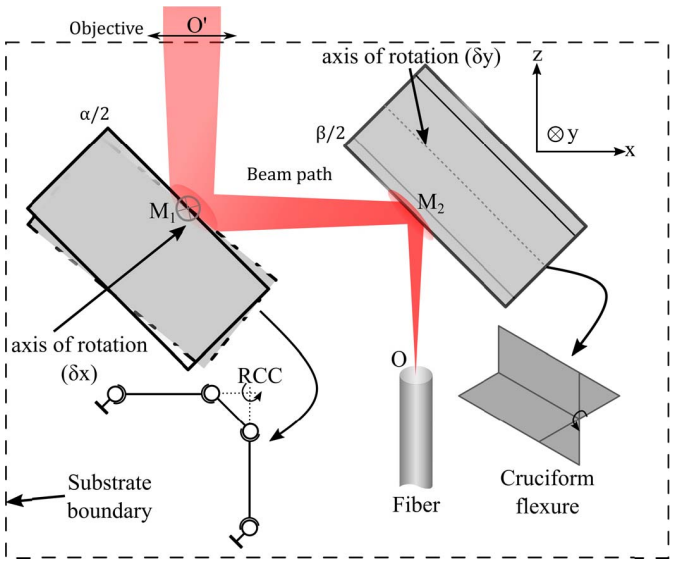

Fig. 3. Schematic of the beam path. A collimated output is focused (using an objective) and guided on the end facet of the fiber using two micromachined mirrors. The mirrors are remotely adjusted using a femtosecond laser to scan the fiber face in the *xy* plane. The deformed state is drawn underneath.

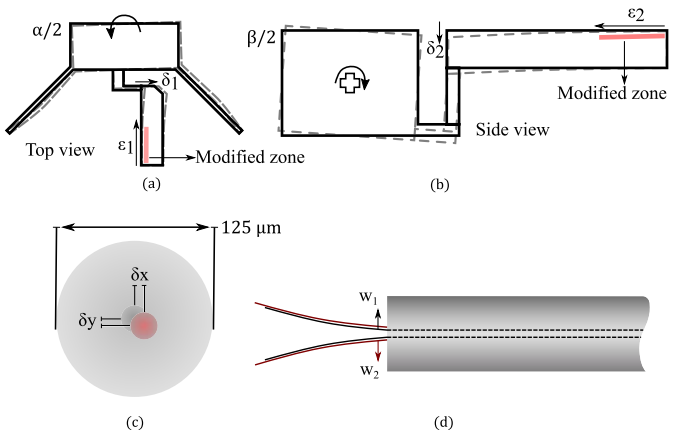

Fig. 4. (a) and (b) Visual representation of the actuation mechanism. Laser-written lines are placed in strategic locations in the bulk of the actuator creating a permanent strain (ε) in the modified zone and a net displacement (δ) at the tip of the actuator. Using flexures, this linear displacement can drive more complex movements at the end-effector. (c) and (d) Graphical representation of the misalignment between the laser mode and fiber mode and their modal diameters.

with a center of rotation at the geometrical center of M_1. Two flexible elements (cantilevers) intersecting on M_1 enable the mechanism to rotate about the y-axis. This allows scanning the focus along the x-direction. The second mirror (M_2) sits on a torsion mechanism supported by two cruciform flexures on either side forming an axis of rotation along their intersection. By titling the mechanism about this axis and thus M_2, the focus can be scanned along the y-direction. Unlike the RCR mechanism, the rotation is offset from the mirror surface. This results in a parasitic translation of the mirror surface. However, for small angles (as is the case here), this parasitic effect is negligible.

B. Actuation Principle and Mechanism

The working principle of the device is based on femtosecond laser-induced volume variation in combination with flexure-based guidance mechanisms. Under a specific set of laser parameters, such as pulse width and pulse energy, femtosecond laser modifications consist of self-organized porous structures known as *nanogratings* [35]. These structures exhibit a marginal increase in the overall volume of the modified zone [32], resulting in anisotropic stresses in the neighboring bulk material [36], [37]. The magnitude of this expansion depends on exposure parameters, such as pulse energy and deposited energy, but typically varies between 0.01% and 0.05% of the exposed volume. The orientation of these nanogratings can also be changed by varying the polarization of the writing beam [37], [38]. By combining such volume changes with flexure-based guidance mechanisms [39], [40], a variety of movements can be driven almost anywhere and away from the actuator.

To adjust M_1, laser-affected zones (LAZ-modified region consisting of several laser-written lines) are inscribed near the sidewalls of the actuator, as shown in Fig. 4(a). By adding more lines on top of each other and, subsequently, stitching modified planes next to each other, the overall volume expansion is further enhanced in a controlled manner. This creates bimorph element - layers of modified and unmodified material within the actuator, forcing it to bend and rotate the mirror. The position of the modified zone within the actuator defines the direction of rotation, i.e., depending on whether the left- or right-hand side of the actuator is modified, the mirror can rotate counterclockwise or clockwise, respectively.

Similarly, to adjust M_2, LAZs are written inside the bulk of the actuator near its top and bottom surfaces, as shown in Fig. 4(b). Depending on their position, the free end of the actuator can either bend up or down, just like a bimorph structure, thus rotating the mirror in a bidirectional manner. Given the marginally small strain produced in the modified zone (a few tens of nanometers), the length of the actuator acts as an amplification mechanism, driving larger movements at its free end.

Under small-angle approximation, the offsets δx and δx can be written as

$$\delta x = (M_1M_2 + M_2O) \times \alpha \tag{1}$$

and

$$\delta y = (M_2O) \times \beta \tag{2}$$

where $\alpha/2$ and $\beta/2$ denote the rotations of M_1 and M_2, respectively. The points M_1, M_2, and O are indicated in Fig. 3.

By approximating the incoming beam as a Gaussian field on the face of the fiber (i.e., with a zero longitudinal offset along z), the power transmission coefficient through the fiber can be written as [41], [42]

$$T = \left(\frac{2w_1w_2}{w_1^2 + w_2^2}\right)^2 \exp\left[\frac{-2\left(\delta x^2 + \delta y^2\right)}{w_1^2 + w_2^2}\right] \tag{3}$$

where w_1 and w_2 denote the modal diameter ($1/e^2$) of the focusing beam and fiber, respectively. The angles α and β can be extracted simply through trigonometric relations from

TABLE I
ACTUATOR AND FLEXURE DIMENSIONS (IN MM)

Mechanism	W	D	H	w	d	h
Fig. 5 (a)	0.7	5	1	0.1	3	1
Fig. 5 (b)	2	4	0.35	0.7	0.1	0.3

their respective actuator displacements δ_1 and δ_2. However, the relationship between tip deflection (δ) and strain (ε) is much more complicated and can be found in [43] and [44]. Note that, in (3), no angular offset is assumed between the two fields.

C. Simulations of the Individual Degrees of Freedom

The range of motion of both mechanisms is dependent on the magnitude of volume variation within the modified region. As mentioned earlier, this strain is a fraction of the modified volume and can result in only a few tens of nanometers in linear displacement. Although this can be further enhanced by optimizing the writing parameters, the dimensions of the flexures and the actuator play a crucial role in determining the overall range of motion.

In this finite-element modeling (FEM) analysis (realized using Comsol Multiphysics), the angle of rotation is chosen as a metric function, which is then maximized with respect to the flexure real estate. This is achieved by minimizing the combined stiffnesses of the individual elements at the point of interest (center/axis of rotation). A similar analysis is also carried for dimensioning the actuator. As is evident from the design, this can be achieved by reducing the bending stiffness of the actuator—if the bending stiffness is lower, the displacement of the free end will be larger. However, when coupled with the stiffness of the rest of the mechanism, below a certain bending stiffness, the actuator is too weak to transfer sufficient force and buckles along its length. The results of this analysis are shown in Fig. 5.

Based on these simulations, the optimized dimensions are noted in Table I. The actuator dimensions are selected based on the analysis shown in Fig. 5(c) and (d). Inherent to both designs, the actuator depth acts as an amplification mechanism. This is evident from the simulations as a longer depth results in a bigger rotation angle. However, this is accompanied by lower vibrating modes making the device more sensitive to surrounding vibrations. As a compromise, the dimensions of the actuator are chosen from the bottom-left region of the innermost contour of these plots. In this region, the fundamental mode lies at 18 kHz, which is reasonably near the upper limit of usual acoustic vibrations. By using thicker substrates, reducing the overall size (mass) of the mechanism, and depending on the desired range of motion, the fundamental mode frequency can be increased several times or even by an order of magnitude.

An important aspect in the design phase is the stress within flexures and in the modified zone. Stress-accelerated corrosion of glasses by water vapor is a known phenomenon [45], [46],

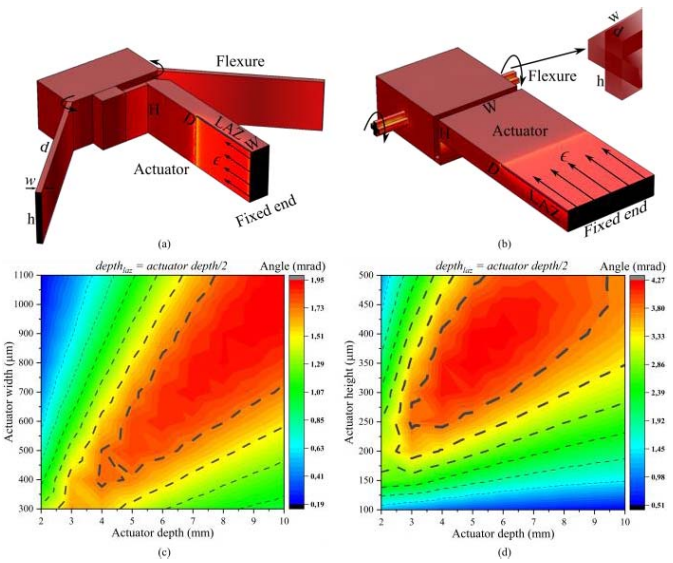

Fig. 5. FEM simulation results for optimization of actuator dimensions of the adjustable mirrors. (a) RCC mechanism of part A in Fig. 2. Here, the modified zone is simulated on the left wall of the actuator resulting in a bimorph element. The volume expansion results in a permanent strain, which is transferred through a flexible element to the rest of the mechanism. (b) Vertical degree of freedom mechanism marked as B in Fig. 2. Here, the patterns are placed just below the top surface of the actuator forcing a downward motion of the other end. A flexible element couples the motion to the rest of the mechanism. (c) and (d) Resulting angles of the two mechanisms as a function of the actuator dimensions. The dotted lines represent contours of equal angle.

which is further enhanced at high levels of stress, temperature, and humidity. However, in our case, the maximum stress level is less than 100 MPa (by design). At these stress levels and under normal laboratory conditions, a stable stress state is observed [47].

III. EXPERIMENTAL RESULTS

A. Fabrication and Assembly

The complete device is fabricated in a single step using femtosecond laser machining combined with wet chemical etching. The full details of the process can be found in [48], but a brief description is given here. A substrate of fused silica is mounted on precise $x-y$ positioning stages, and the contour of the device is drawn and stitched together layer-by-layer in a bottom-to-top approach. For this step, a laser (from Amplitude Systèmes) delivering 270-fs pulses at a wavelength of 1030 nm is used. To outline the contour, the sample is translated at a speed of 8 mm/s under the focus while maintaining constant deposited energy of 12 J/mm^2. In a subsequent step, the sample is etched in a dilute acid bath (2.5% HF) for about 24 h.

For this demonstration, we fabricate custom-made mirrors using the same process out of a 250-μm-thick substrate of fused silica. After etching, the mirrors are coated using a conventional gold sputterer and glued to the outer walls of the mirror surfaces defined on the substrate. As mentioned in Section I, various approaches can be used to remove the need for adding mirrors without changing the underlying principle.

To install the fiber, it is fixed on a linear stage and aligned with the v-groove. It is then slowly drawn into the v-groove by

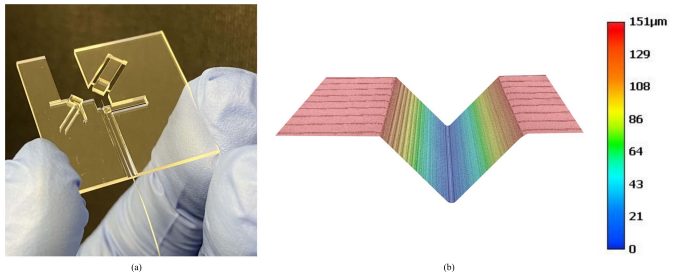

Fig. 6. (a) Fully assembled device is shown here without the glued mirrors. (b) Height profile of the laser manufactured v-groove

translating the stage toward the sample. As the fiber arrives at the end of the groove, the clamp is lifted, and the fiber is slid under it. The clamp is then released to make contact with the top surface of the cladding, thus forcing two contact points on the sidewalls of the v-groove. The rest of the fiber is then glued using UV curing glue. The assembled mechanism is shown in Fig. 6.

B. Geometrical Optimization of Laser-Written Patterns

The volume enhancement inside the modified zone is not only dependent on laser parameters but also on how the patterns are inscribed and distributed inside the bulk of the material. Relying on an earlier study about optimized laser parameters [44], in the following, we investigate the effect of the distribution of LAZs.

To quantify the strain, we use an indirect approach relying on measuring the angle of rotation. For this, we use an optical triangulation method by reflecting a laser off the micromachined mirrors and monitor its position on a position sensing device (PSD). The angle of rotation can be backcalculated by monitoring the displacement of the reflected beam in the plane of the sensor. Further details can be found in [49].

To optimize the inscription process, different exposure strategies are employed by changing the geometry of the patterns within the bulk of the actuators. Between these methods, the overall strain within the LAZ varies, thus resulting in different angles of rotation. In our first approach, called horizontal writing vertical stacking and shown in Fig. 7(a), the sample is translated under the focusing objective, and laser-written lines are stacked laterally in one horizontal plane resulting in a plane of the modified zone. Afterward, the focusing objective is moved upward, and similar planes are stitched together vertically through the thickness of the actuator. The width of each plane is half the actuator width and extends up to the neutral plane of the actuator. The lateral separation between two lines and the vertical separation between two planes is set at 10 μm.

Our second method, called vertical writing horizontal stacking, as shown in Fig. 7(b), involves stacking the individual lines vertically on top of each other creating a wall of LAZ. Next, in a bottom-to-top approach, similar patterns are deposited next to each other. Although the overall modified zone looks similar to before, the net strain is significantly reduced. This is due to the laser beam interference with

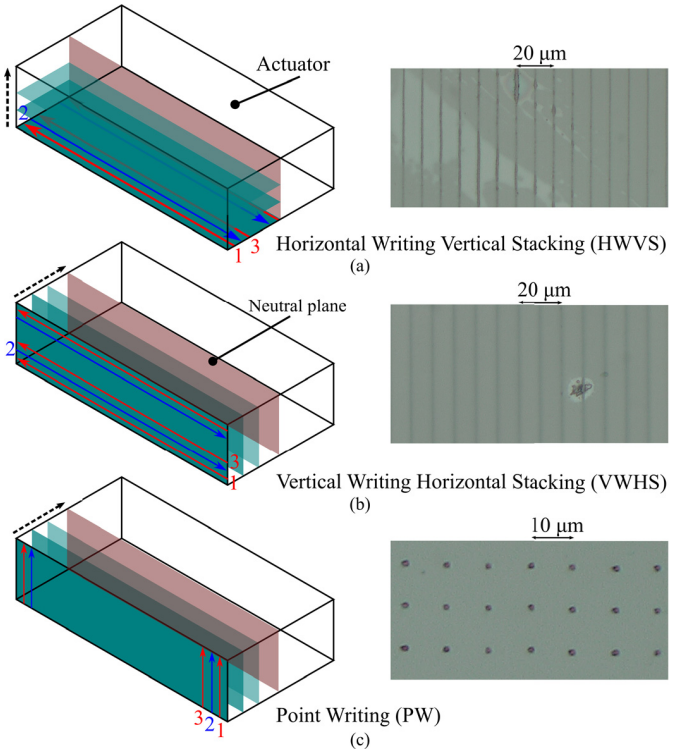

Fig. 7. Visual representation of the different writing schemes used in these experiments. (a) Lines are written along with the actuator in either until the neutral plane. The same process is then repeated for subsequent planes. (b) Individual lines are written vertically on top of each other from bottom to top, and then, similar patterns are repeated until the neutral plane. (c) Hybrid writing scheme that involves translating the sample and the focusing objective. The focus is translated along with the sample thickness, and similar patterns are then repeated in a matrix form.

already existing patterns. Except for the first plane, the laser beam passes through an interface of modified and unmodified material. This distorts the focal plane and significantly reduces the overall strain. The spacing between lines and planes is unchanged.

Finally, in the third method, called point writing and shown in Fig. 7(c), the laser focus is translated through the thickness of the sample while keeping the sample stationary. Next, the sample is translated, and a similar pattern is written in the next position. In this manner, a matrix of points is generated in the plane of the substrate as shown in the figure. Here too, the presence of modified material affects each subsequent LAZ. Besides, the fraction of modified volume is significantly smaller in comparison to the other two methods.

For the RCR mechanism shown in Fig. 5(a), laser-exposed patterns are written alongside the sidewall of the actuator. For comparison, all three writing methods are used. A similar set of experiments is performed using the cruciform mechanism shown in Fig. 5(b). By following the first writing method (HWVS), LAZs are written along the width of the actuator slightly below its top surface and away from the edges. For these experiments, the spacing between two individual lines is reduced to 2 μm, while the separation between planes is maintained at 10 μm. Between planes, the laser is switched OFF for a short while to distinguish them from each other.

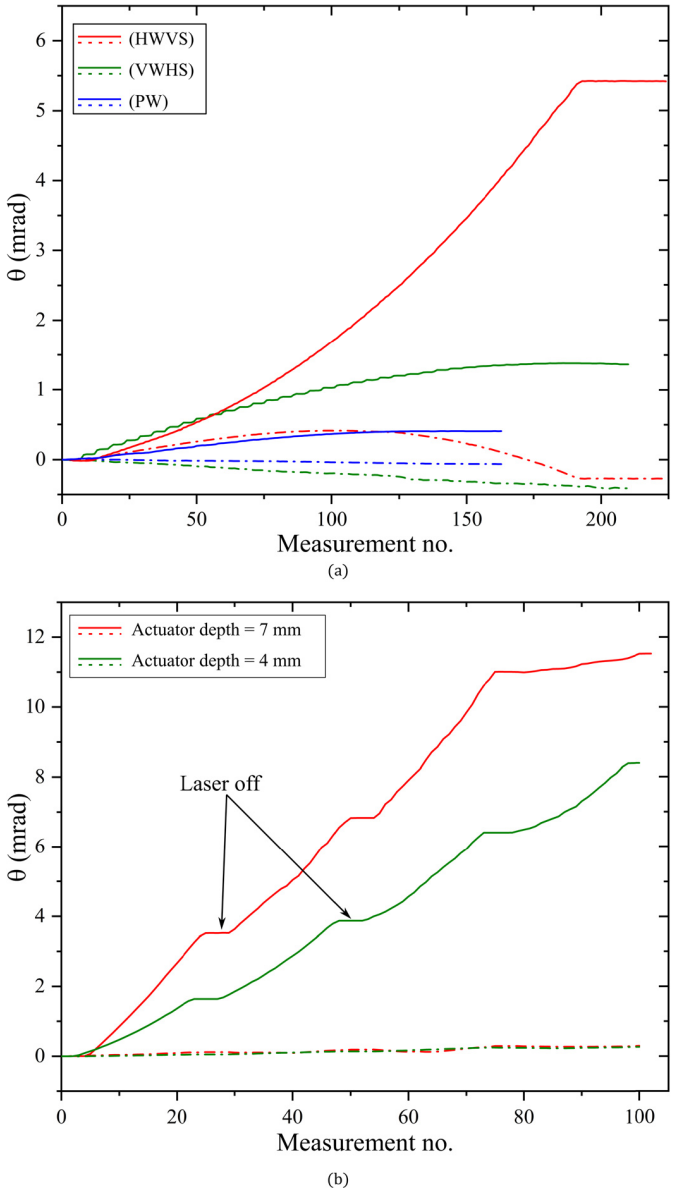

Fig. 8. (a) Experimental results of the in-plane angles (solid lines) between the three methods. A maximum adjustment of 5.4 mrad is obtained using the patterns in Fig. 7 (a) in comparison 1.4 and 0.4 mrad using (b) and (c), respectively. Due to the bottom-to-top writing approach, a parasitic bending of the actuator is also observed, which can be compensated by varying the power or density of the patterns while approaching the top surface. This is indicated by the respective dashed lines. (b) Out-of-plane adjustment is plotted for two different actuator depths. Four layers of LAZ are written within the bulk of the actuator. Between layers, the laser is turned off, indicated by the stagnant region of the curves. The parasitic movement is plotted with a dashed line.

The results are shown in Fig. 8. For these experiments, a femtosecond laser emitting 300-fs pulses at a repetition rate of 300 kHz is used. The pulse energy is fixed at 220 nJ with the writing speed set at 4.5 mm/s, leading to a dose of 12 J/mm^2. The polarization is parallel to the writing direction.

C. Fiber Injection Experiment

Our goal is to demonstrate a key element of the laser diode packaging process—a high-efficiency injection from a laser beam into an SMF. As an extension to this work and following the same repositioning methodology, the laser diode together with the beam conditioning optics can be mounted on the same substrate.

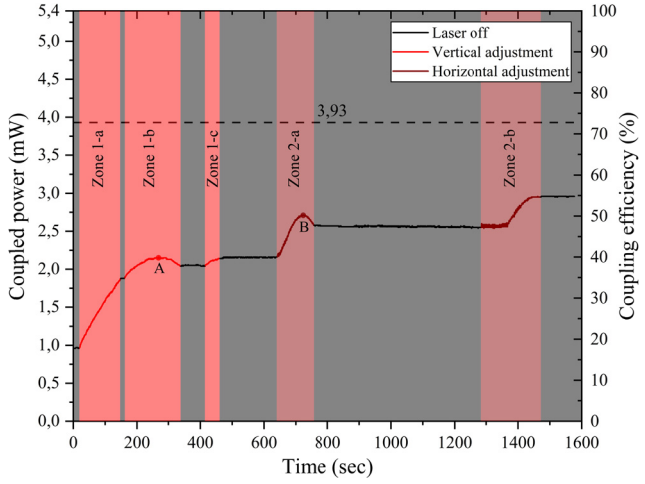

Fig. 9. Output power as a function of time. The writing is divided into two zones. In zone-1, vertical adjustment is done followed by horizontal adjustment in zone-2. Note that the writing time is not optimized as the alignment algorithm is implemented manually.

For this experiment, a collimated output of a fiber pigtailed laser diode at 980 nm is used as a light source. Using a long working distance objective (Mitutoyo, 20X), the beam is reflected off the adjustable mirrors and focused on the fiber end, as shown in Fig. 3. The glass chip holding the fiber is then coarsely aligned using positioning stages until some power is observed at the output. Next, fine adjustments are done to maximize the output power and, thus, the coupling efficiency. This step is repeated multiple times to maximize coupling into the fiber mode. Once in its optimal position, the fiber is misaligned by shifting the chip with respect to the focusing lens. The shifts are approximately 3 μm along the x-axis and 4.5 μm along the y-axis. This results in a drop in output power, mimicking postassembly alignment errors in a diode package. To optimize coupling again, a noncontact adjustment is carried out by writing patterns inside both actuators. While writing, the coupled power serves as an assembly function and is monitored simultaneously and maximized along the two axes. The writing is stopped when the maximum output power level is reached. The results are shown in Fig. 9. In this experiment, the fiber is an SMF (SM-980-G80 from Thorlabs) with an average mode field diameter of 4.5 μm at 980 nm. The focusing objective has a 0.4 NA and a working distance of 20 mm.

The noncontact adjustment is done in a two-step process.

Step 1: Starting with the y-axis alignment, the actuator is modified just below its top surface, resulting in an immediate increase in power indicated by zone 1-a. The writing is continued through zone 1-b, and a second plane is added on top until the optimal position is crossed and a drop in power is observed. This is indicated by point A in the plot. At this point, the femtosecond laser is switched OFF (black region), and the focus is moved near the bottom surface. Here, further patterns are written tilting the mirror in the opposite direction

TABLE II
SIZE OF THE POSITIONING WINDOW (IN MICROMETERS)

Axis	Correction done	Potential range
X	3	45
Y	4.5	15

and toward the optimal position, as shown in zone 1-c. The process is stopped as soon as the earlier power level (point A) is retrieved. Afterward, the laser is turned off again, and the device is translated to begin the x alignment.

Step 2: In this next step, the actuator of the RCR mechanism is modified for horizontal adjustment. This is done by writing lines along the length of the actuator near its edge. As lines are written in zone 2-a, the coupled power begins to increase further, reaches a maximum (point B), and then decreases. Here, the writing process is stopped again, and the device is translated to modify the opposite wall of the actuator. During this time, the coupled power stays constant as indicated by the black region on the plot. In zone 2-b, further exposure reorients the mirror back toward the optimal position, resulting in a further increase in power. The alignment is stopped when the power level saturates at a coupling efficiency of 54.8%. The modified device is shown in Fig. 10. To validate the coupling, the chip is realigned using a six-axis precise positioning stage (OptoSigma-DAU-080M-R). The stage has a linear resolution of 0.5 μm and an angular resolution of approximately 8 mrad. After repeated attempts, the coupling efficiency is the same as before.

Although we are correcting for relatively small misalignments in this proof-of-concept experiment, the actual range of motion capability of the device is significantly larger, as shown in Fig. 8. At the fiber position, this corresponds to a positioning window whose size is also dependent on the focal length of the coupling lens. In the specific case of our device, the size of the positioning window is given in Table II.

In addition to laser parameters, the strain within the actuators and, consequently, their range of motion also depend on the fraction of modified volume. For example, in the results of Fig. 8(a), the modified volume is 50% of the overall actuator volume, whereas it is only 5% in Fig. 8(b). Similarly, the fiber coupling in this experiment was achieved by modifying less than 2% of the actuator volume. Therefore, the actual range of motion is far greater than what is corrected here. Furthermore, by inducing densification [50] in part of the actuator, the range of motion can potentially be doubled. However, a limiting factor in doing so is the peak stress within the flexures or the modified zones. While staying below a conservative stress level of 100 MPa, we provide the maximum range of motion indicated in Table II. Depending on the application and desired range of motion, the footprint of the device can be further optimized.

D. Loss Analysis

To quantify the losses occurring within the mechanism, we mount the fiber directly in front of the objective (without the mechanism). In this case, the output power is measured at 3.93 mW, nearly an 18% increase in coupling efficiency. To account for this difference, we measure the losses occurring at the two interfaces within the device. The reason for these losses is twofold. On the first mirror, the beam size is slightly bigger than the mirror diameter resulting in clipping loss. In addition, there is a certain amount of reflection loss on both mirrors. This results in a reduction in optical power at the fiber input. Due to physical constraints, these losses cannot be measured easily on the chip, so we measure them separately. The results are shown in Table III.

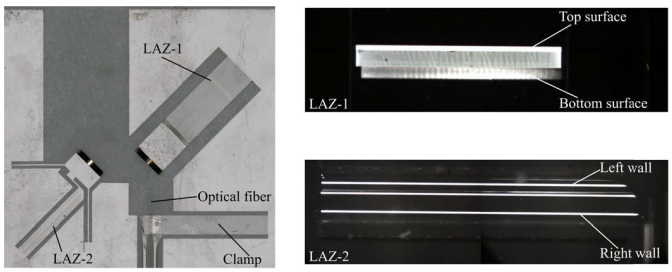

Fig. 10. (a) Optical image of the device after laser adjustment showing the modified region in the actuators. (b) Cross-polarized microscope image revealing the form birefringence in the modified zone. LAZs are offset from the nearest edge by 100 μm and buried 30 μm away from the top and bottom surfaces to prevent effects, such as clipping of the laser beam while writing or local ablation.

TABLE III
BUDGET OF MEASURED LOSSES FOR THE DIFFERENT INTERFACES

Interface	Clipping loss (%)	Reflection loss (%)
M_1	6.34 ± 1	5.69 ± 0.8
M_2	0	5.69 ± 0.8

The summation of these losses nearly matches the observed difference. This confirms that, by discounting the losses induced by the mirrors, the mechanism can attain the same coupling efficiency as is possible with commercially available high-resolution fiber positioning stages.

IV. CONCLUSION

Packaging of optical components into a reliable and robust assembly can prove to be a major bottleneck in the commercialization of different photonic devices. The microassembly of small components with sub-μm tolerances requires task-specific and expensive alignment machinery. Furthermore, assembly methods at the macroscale are not easily transferable to the microscale. Therefore, packaging costs, which involve the handling of components, actuation, alignment, fixation, and so on, and depending on the number of individual components, can constitute a major portion of the overall production cost. In comparison, fabricating devices out of a single monolith brings advantages not only in terms of device miniaturization but also benefits from lesser components and assembly steps, prealigned markers, packaging robustness, and superior performance.

In this work, taking advantage of precision machined mirrors and v-grooves, together with embedded fine positioning elements activated by femtosecond laser exposure, we have demonstrated a two-degree-of-freedom fiber injection mechanism. A correction of 3 μm along the x-axis and 4.5 μm along the y-axis was achieved. However, the potential size of the correction window is much larger, thus significantly relaxing tolerances during assembly. From a packaging perspective, for a fully integrated device where the laser diode is mounted on the chip itself together with a coupling lens (or additional components), the device would be able to compensate for typical assembly errors. For instance, and as a practical illustration, if the coupling lens is mounted near O' in Fig. 3, alignment errors up to 45 μm along the x-axis and 15 μm along the y-axis could be corrected.

Although shown here for a two-degree-of-freedom element, the concept can be extended to adjust additional degrees of freedom and expanded to other kinematics, such as parallel ones, possibly further miniaturizing the real estate, without changing the underlying positioning methodology.

The actuation method relies on a nonlinear laser absorption process to induce subnanoscale modifications in the bulk of the substrate that, when combined with flexure-based kinematic mechanisms, forms a permanent actuator with a sub-nm resolution. The process further benefits from excellent mechanical and thermal properties offered by the substrate material (fused silica having the lowest CTE among nonengineered materials), high-precision prealignment between individual components, and an integrated functionality allowing for controlled actuation, thus relaxing assembly tolerances. Among the currently available manufacturing techniques, the combination of femtosecond laser exposure and chemical etching offers the highest flexibility in terms of 3-D design capability. Nevertheless, the femtosecond laser-tuning method is generic and could be applied to other devices made out of glass and manufactured by other means.

Although the method introduces an additional process step, depending on the use case, the process cost can be balanced by the benefits obtained in terms of the final device performance, e.g., better coupling efficiency, device robustness, and thermally stable package. It can find applications in a variety of problems related to photonic devices, such as fiber-laser cavities, Fabry–Pérot resonators, quantum optics devices, and, in particular, PIC's packaging.

REFERENCES

[1] C. R. Doerr, "Silicon photonic integration in telecommunications," *Frontiers Phys.*, vol. 3, p. 37, Aug. 2015.

[2] A. W. Elshaari, W. Pernice, K. Srinivasan, O. Benson, and V. Zwiller, "Hybrid integrated quantum photonic circuits," *Nature Photon.*, vol. 14, pp. 285–298, May 2020.

[3] M. C. Estevez, M. Alvarez, and L. M. Lechuga, "Integrated optical devices for lab-on-a-chip biosensing applications," *Laser Photon. Rev.*, vol. 6, no. 4, pp. 463–487, Jul. 2012.

[4] J. Leuthold, C. Koos, and W. Freude, "Nonlinear silicon photonics," *Nature Photon.*, vol. 4, no. 8, pp. 535–544, Aug. 2010.

[5] A. L. Gaeta, M. Lipson, and T. J. Kippenberg, "Photonic-chip-based frequency combs," *Nature Photon.*, vol. 13, no. 3, pp. 158–169, Mar. 2019.

[6] L. Carroll *et al.*, "Photonic packaging: Transforming silicon photonic integrated circuits into photonic devices," *Appl. Sci.*, vol. 6, no. 12, pp. 426–446, 2016.

[7] J. Hwan Song, H. N. J. Fernando, B. Roycroft, B. Corbett, and F. H. Peters, "Practical design of lensed fibers for semiconductor laser packaging using laser welding technique," *J. Lightw. Technol.*, vol. 27, no. 11, pp. 1533–1539, Jun. 2009.

[8] D. Taillaert *et al.*, "An out-of-plane grating coupler for efficient butt-coupling between compact planar waveguides and single-mode fibers," *IEEE J. Quantum Electron.*, vol. 38, no. 7, pp. 949–955, Aug. 2002.

[9] J. R. Kim and A. Siahmakoun, "Evanescent coupling to silicon waveguides using surface plasmon polaritons," *Appl. Opt.*, vol. 59, no. 13, pp. 64–68, 2020.

[10] R. Marchetti, L. C. , L. Carroll, K. Gradkowski, and P. Minzioni, "Coupling strategies for silicon photonics integrated chips," *Photon. Res.*, vol. 7, no. 2, pp. 201–239, 2019.

[11] P. De Dobbelaere *et al.*, "Packaging of silicon photonics systems," in *Proc. Opt. Fiber Commun. Conf.*, 2014, p. W3I-2.

[12] S. J. Mcnab, N. Moll, and Y. A. Vlasov, "Ultra-low loss photonic integrated circuit with membrane-type photonic crystal waveguides," *Opt. Exp.*, vol. 11, no. 22, pp. 2927–2939, 2003.

[13] L. Carroll, D. Gerace, I. Cristiani, S. Menezo, and L. C. Andreani, "Broad parameter optimization of polarization-diversity 2D grating couplers for silicon photonics," *Opt. Exp.*, vol. 21, no. 18, pp. 21556–21568, 2013.

[14] R. Dangel *et al.*, "Polymer waveguides for electro-optical integration in data centers and high-performance computers," *Opt. Exp.*, vol. 23, no. 4, pp. 4736–4750, 2015.

[15] S. Maruo, O. Nakamura, and S. Kawata, "Three-dimensional microfabrication with two-photon-absorbed photopolymerization," *Opt. Lett.*, vol. 22, no. 2, pp. 132–134, 1997.

[16] S. Kawata, H.-B. Sun, T. Tanaka, and K. Takada, "Finer features for functional microdevices," *Nature*, vol. 412, no. 6848, pp. 697–698, Aug. 2001.

[17] G. Cojoc *et al.*, "Optical micro-structures fabricated on top of optical fibers by means of two-photon photopolymerization," *Microelectronic Eng.*, vol. 87, nos. 5–8, pp. 876–879, May 2010.

[18] M. Malinauskas *et al.*, "Femtosecond laser polymerization of hybrid/integrated micro-optical elements and their characterization," *J. Opt.*, vol. 12, no. 12, Dec. 2010, Art. no. 124010.

[19] Y. Lin, J. Guo, A. A. Shapiro, and F. G. Shi, "WIAD minimization in butterfly laser module packages: Clip design," *IEEE Trans. Adv. Packag.*, vol. 30, no. 3, pp. 499–505, Aug. 2007.

[20] Y.-C. Hsu, Y.-C. Tsai, J.-H. Kuang, M.-T. Sheen, P.-H. Hsu, and W.-H. Cheng, "A notch-saddle-compensation technique in butterfly-type laser module packages," *J. Lightw. Technol.*, vol. 25, no. 6, pp. 1594–1601, Jun. 2007.

[21] Y. Lin, C. Eichele, and F. G. Shi, "Effect of welding sequence on welding-induced-alignment-distortion in packaging of butterfly laser diode modules: Simulation and experiment," *J. Lightw. Technol.*, vol. 23, no. 2, pp. 615–623, Feb. 2005.

[22] M. H. M. van Gastel, P. C. J. N. Rosielle, and M. Steinbuch, "A concept for accurate edge-coupled multi-fiber photonic interconnects," *J. Lightw. Technol.*, vol. 37, no. 4, pp. 1374–1380, Feb. 15, 2019.

[23] M. S. Cohen *et al.*, "Packaging of high-density fiber/laser modules using passive alignment techniques," in *Proc. 42nd Electron. Compon. Technol. Conf.*, San Diego, CA, USA, 1992, pp. 98–107.

[24] M. J. Wale and C. Edge, "Self aligned, flip chip assembly of photonic devices with electrical and optical connections," *IEEE Trans., Comp., Hybrids, Manufact. Technol.*, vol. 13, no. 4, pp. 780–786, May 1990.

[25] K. Ishikawa, J. Zhang, A. Tuantranont, V. M. Bright, and Y.-C. Lee, "An integrated micro-optical system for VCSEL-to-fiber active alignment," *Sens. Actuators A, Phys.*, vol. 103, nos. 1–2, pp. 109–115, Jan. 2003.

[26] O. Solgaard, M. Daneman, N. C. Tien, A. Friedberger, R. S. Müller, and K. Y. Lau, "Optoelectronic packaging using silicon surface-micromachined alignment mirrors," *IEEE Photon. Technol. Lett.*, vol. 7, no. 1, pp. 41–43, Jan. 1995.

[27] M. J. Daneman, O. Solgaard, N. C. Tien, K. Y. Lau, and R. S. Müller, "Laser-to-fiber coupling module using a micromachined alignment mirror," *IEEE Photon. Technol. Lett.*, vol. 8, no. 3, pp. 396–398, Mar. 1996.

[28] V. A. Henneken, W. P. Sassen, W. van der Vlist, W. H. A. Wien, M. Tichem, and P. M. Sarro, "Two-dimensional fiber positioning and clamping device for product-internal microassembly," *J. Microelectromech. Syst.*, vol. 17, no. 3, pp. 724–734, Jun. 2008.

[29] M. Tichem, B. Karpuschewski, and P. M. Sarro, "Self-adjustment of micro-mechatronic systems," in *Proc. Ann. CIRP*, 2003, pp. 17–20.

[30] K. G. P. Folkersma, D. M. Brouwer, G. R. B. E. Römer, and J. L. Herder, "Robust precision alignment algorithm for micro tube laser forming," *Precis. Eng.*, vol. 46, pp. 301–308, Oct. 2016.
[31] G. Folkersma, G.-W. Römer, and D. Brouwer, "In-plane laser forming for high precision alignment," *Opt. Eng.*, vol. 53, no. 12, pp. 126105–126116, 2014.
[32] A. Champion and Y. Bellouard, "Direct volume variation measurements in fused silica specimens exposed to femtosecond laser," *Opt. Mater. Exp.*, vol. 2, pp. 789–798, Jun. 2012.
[33] Y. Bellouard, "Non-contact sub-nanometer optical repositioning using femtosecond lasers," *Opt. Exp.*, vol. 23, pp. 29258–29267, Nov. 2015, doi: 10.1364/OE.23.029258.
[34] K. M. Nowak, H. J. Baker, and D. R. Hall, "Efficient laser polishing of silica micro-optic components," *Appl. Opt.*, vol. 45, no. 1, pp. 162–171, 2006.
[35] Y. Shimotsuma, P. G. Kazansky, J. Qiu, and K. Hirao, "Self-organized nanogratings in glass irradiated by ultrashort light pulses," *Phys. Rev. Lett.*, vol. 91, no. 24, pp. 247405–247408, Dec. 2003.
[36] B. Mcmillen and Y. Bellouard, "On the anisotropy of stress-distribution induced in glasses and crystals by non-ablative femtosecond laser exposure," *Opt. Exp.*, vol. 23, no. 1, pp. 86–100, 2015.
[37] A. Champion, M. Beresna, P. Kazansky, and Y. Bellouard, "Stress distribution around femtosecond laser affected zones: Effect of nanogratings orientation," *Opt. Exp.*, vol. 21, no. 21, pp. 24942–24951, 2013.
[38] C. Hnatovsky, R. S. Taylor, E. Simova, V. R. Bhardwaj, D. M. Rayner, and P. B. Corkum, "Polarization-selective etching in femtosecond laser-assisted microfluidic channel fabrication in fused silica," *Opt. Lett.*, vol. 30, no. 14, pp. 1867–1869, 2005.
[39] Y. Bellouard, A. A. Said, and P. Bado, "Integrating optics and micro-mechanics in a single substrate: A step toward monolithic integration in fused silica," *Opt. Exp.*, vol. 13, pp. 6635–6644, Aug. 2005.
[40] Y. Bellouard, "On the bending strength of fused silica flexures fabricated by ultrafast lasers," *Opt. Mater. Exp.*, vol. 1, pp. 816–831, Sep. 2011.
[41] D. Marcuse, "Loss analysis of single-mode fiber splices," *Bell Syst. Tech. J.*, vol. 56, no. 5, pp. 703–718, May 1977.
[42] S. Nemoto and T. Makimoto, "Analysis of splice loss in single-mode fibres using a Gaussian field approximation," *Opt. Quantum Electron.*, vol. 11, no. 5, pp. 447–457, Sep. 1979.
[43] P. Vlugter, E. Block, and Y. Bellouard, "Local tuning of fused silica thermal expansion coefficient using femtosecond laser," *Phys. Rev. Mater.*, vol. 3, no. 5, p. 53802, May 2019.
[44] Y. Bellouard *et al.*, "Stress-state manipulation in fused silica via femtosecond laser irradiation," *Optica*, vol. 3, no. 12, pp. 1285–1293, 2016.
[45] S. M. Wiederhorn, "Influence of water vapor on crack propagation in soda-lime glass," *J. Amer. Ceram. Soc.*, vol. 50, no. 8, pp. 407–414, Aug. 1967.
[46] S. M. Wiederhorn, S. W. Freiman, E. R. Fuller, and C. J. Simmons, "Effects of water and other dielectrics on crack growth," *J. Mater. Sci.*, vol. 17, no. 12, pp. 3460–3478, Dec. 1982.
[47] C. E. Athanasiou, "Non-contact femtosecond laser-based methods for investigating glass mechanics at small scales," Ph.D. dissertation, Doctoral School Photon., Ecole Polytechnique Fédérale de Lausanne, Lausanne, Switzerland, 2018.
[48] Y. Bellouard, A. Said, M. Dugan, and P. Bado, "Fabrication of high-aspect ratio, micro-fluidic channels and tunnels using femtosecond laser pulses and chemical etching," *Opt. Exp.*, vol. 12, no. 10, pp. 2120–2129, 2004.
[49] S. I. Nazir and Y. Bellouard, "A monolithic gimbal micro-mirror fabricated and remotely tuned with a femtosecond laser," *Micromachines*, vol. 10, no. 9, pp. 611–627, 2019.
[50] Y. Bellouard, T. Colomb, C. Depeursinge, M. Dugan, A. A. Said, and P. Bado, "Nanoindentation and birefringence measurements on fused silica specimen exposed to low-energy femtosecond pulses," *Opt. Exp.*, vol. 14, no. 18, pp. 8360–8366, 2006.